Julia Hesse | Dennis T. Klier | Massimo Sgarzi | Anne Nsubuga
Christoph Bauer | Jörg Grenzer | René Hebner | Marcus Wislicenus
Tanmaya Joshi | Michael U. Kumke | Holger Stephan

Rapid synthesis of sub-10 nm hexagonal $NaYF_4$-based upconverting nanoparticles using Therminol® 66

Suggested citation referring to the original publication:
ChemistryOpen 7 (2018) pp. 159–168
DOI https://doi.org/10.1002/open.201700186
ISSN 2191-1363

ChemPubSoc Europe

DOI: 10.1002/open.201700186

Open Access ChemistryOPEN Full Papers

Rapid Synthesis of Sub-10 nm Hexagonal $NaYF_4$-Based Upconverting Nanoparticles using Therminol® 66

Julia Hesse[+],[a] Dennis T. Klier[+],[b] Massimo Sgarzi,[a] Anne Nsubuga,[a] Christoph Bauer,[c] Jörg Grenzer,[d] René Hübner,[d] Marcus Wislicenus,[e] Tanmaya Joshi,*[a] Michael U. Kumke,*[b] and Holger Stephan*[a]

We report a simple one-pot method for the rapid preparation of sub-10 nm pure hexagonal (β-phase) $NaYF_4$-based upconverting nanoparticles (UCNPs). Using Therminol® 66 as a co-solvent, monodisperse UCNPs could be obtained in unusually short reaction times. By varying the reaction time and reaction temperature, it was possible to control precisely the particle size and crystalline phase of the UCNPs. The upconversion (UC) luminescence properties of the nanocrystals were tuned by varying the concentrations of the dopants (Nd^{3+} and Yb^{3+} sensitizer ions and Er^{3+} activator ions). The size and phase-purity of the as-synthesized core and core–shell nanocrystals were assessed by using complementary transmission electron microscopy, dynamic light scattering, X-ray diffraction, and small-angle X-ray scattering studies. In-depth photophysical evaluation of the UCNPs was pursued by using steady-state and time-resolved luminescence spectroscopy. An enhancement in the UC intensity was observed if the nanocrystals, doped with optimized concentrations of lanthanide sensitizer/activator ions, were further coated with an inert/active shell. This was attributed to the suppression of surface-related luminescence quenching effects.

1. Introduction

Upconverting nanophosphors have the ability to absorb multiple near-infrared (NIR) photons and convert them into shorter-wavelength visible light.[1,2] They show narrow emission and sharp excitation bandwidths, large anti-Stokes' shifts, high chemical, thermal, and photostability, excellent resistance to photobleaching, and low long-term toxicity.[2,3] Due to their unique photophysical properties, upconverting nanoparticles (UCNPs) have potential use in diverse biomedical fields such as bioimaging, photodynamic therapy, and bioanalytics.[4–13] To date, the most frequently studied UCNPs consist of hexagonal closed packed (hcp) β-$NaYF_4$ crystal host lattice co-doped with a sensitizer–activator combination of Ln^{3+} ions (primarily Yb^{3+} combined with Er^{3+}, Tm^{3+}, or Ho^{3+} as activator ions).[14–24] Despite the fact that progress has been made in the synthesis of lanthanide-doped UCNPs, scalable size-controlled production of phase-pure β-$NaYF_4$ nanocrystals still remains a great challenge. In particular, reproducible synthetic routes that can provide access to sub-10 nm nanocrystals with strictly controlled morphology, high crystal phase purity, and exceptional upconversion (UC) luminescence are highly desirable. Reported methods for the synthesis of hcp β-$NaYF_4$ particles with diameters below 10 nm mostly rely on the use of additives such as Gd^{3+} and Eu^{3+} ion in high concentrations. This results in manipulated host lattices, which has a detrimental effect on the luminescent properties of the final materials.[25–29] Other popular strategies to obtain sub-10 nm UCNPs involve the use of an additional high-boiling solvent such as oleylamine (OM)[30] or trioctylphosphine oxide (TOPO)[31–34] in the reaction formulation under harsh synthesis conditions (high temperatures and long reaction times), which limits the choice of compatible solvent systems that can be used.

As part of our quest to develop highly luminescent sub-10 nm UCNPs suitable for imaging applications, herein we

[a] J. Hesse,[+] Dr. M. Sgarzi, A. Nsubuga, Dr. T. Joshi, Dr. H. Stephan
Institute of Radiopharmaceutical Cancer Research
Helmholtz-Zentrum Dresden-Rossendorf
Bautzner Landstraße 400, 01328 Dresden (Germany)
E-mail: t.joshi@hzdr.de
h.stephan@hzdr.de

[b] Dr. D. T. Klier,[+] Prof. Dr. M. U. Kumke
Institute of Chemistry (Physical Chemistry), University of Potsdam
Karl-Liebknecht-Straße 24–25, 14476 Potsdam (Germany)
E-mail: kumke@uni-potsdam.de

[c] C. Bauer
Physical Chemistry, Technische Universität Dresden
Bergstraße 66b, 01062 Dresden (Germany)

[d] Dr. J. Grenzer, Dr. R. Hübner
Institute of Ion Beam Physics and Materials Research
Helmholtz-Zentrum Dresden-Rossendorf
Bautzner Landstraße 400, 01328 Dresden (Germany)

[e] M. Wislicenus
Center Nanoelectronic Technologies
Fraunhofer Institute for Photonic Microsystems
Königsbrücker Straße 178, 01099 Dresden (Germany)

[+] These authors contributed equally to this work

Supporting Information and the ORCID identification number(s) for the author(s) of this article can be found under https://doi.org/10.1002/open.201700186.

report the utilization of Therminol® 66 (T66) as a reaction co-solvent for the synthesis of sub-10 nm phase-pure β-$NaYF_4$ particles. T66 is a commercially available, high-boiling organic fluid that consists of a mixture of terphenyls, hydrogenated terphenyls, and hydrogenated polyphenyls (Figure S1 in the Supporting Information), and it is frequently employed as a heat-transfer liquid.[35–37] Importantly, it is commonly used in industrial processes and has been previously used to prepare quantum dots of various sizes with high reproducibility.[38–40]

Yb^{3+}-sensitized UCNPs are limited in deep-tissue imaging applications, as the absorption peak of Yb^{3+} ions is centered at $\lambda = 980$ nm, which overlaps with the absorption band of water molecules. Moreover, overexposure of biological species with $\lambda = 980$ nm irradiation can cause serious overheating issues, resulting in cell death and tissue damage. Thus, one of our goals was to prepare UCNPs excitable in the first optical transparency window ($\lambda = 650$–950 nm), which is characterized by minimal water absorption and, consequently, offers maximal transparency of blood and organic tissues[41,42] without compromising the UC efficiency.

In this context, previous studies[43] demonstrated that UC under $\lambda = 800$ nm excitation could be achieved through Nd^{3+} co-doping. With the above in mind, we also envisioned using T66 to synthesize sub-10 nm β-$NaYF_4$ UCNPs incorporating Nd^{3+} ions in both the core and shell, obviating the need for any additional phase-transformation steps or additives. The photophysical properties of the individual UCNPs were investigated in detail to illustrate the suitability and versatility of T66 for the controlled synthesis of highly luminescent UCNPs.

2. Results and Discussion

2.1. Morphology and Crystalline Structure

Oleic acid (OA)-stabilized, di- and tri-doped $NaYF_4$ UCNPs, excitable at $\lambda = 980$ and 795 nm, were prepared by a one-pot co-precipitation method by using a suitable combination of $Yb^{3+}/Er^{3+}/Nd^{3+}$ chlorides, ammonium fluoride (NH_4F), and sodium oleate. Reaction in neat T66 resulted in the formation of ultrasmall (≤ 5 nm) cubic-phase particles for all of the time and temperature conditions explored in this study. In comparison, coordinating solvents such as OM and OA are known to favor the growth of pure hexagonal-phase UCNPs.[15,17,44–49] Thus, owing to the superior optical properties of pure hexagonal-phase UCNPs, a binary solvent mixture of T66/OA (3:2, *v*/*v*) was used to obtain sub-10 nm hexagonal UCNPs. To deliver highly luminescent sub-10 nm UCNPs, the Yb^{3+}, Er^{3+}, and Nd^{3+} contents in the core were systematically optimized. Additionally, a few monolayer thick Yb^{3+}/Nd^{3+} (10/25%) active shell was epitaxially grown around the active core by slow injection (feeding rate: 2 mL h^{-1}) of a precursor solution consisting of lanthanide oleates. Construction of an active shell around the luminescent core might serve to enhance the UC luminescence further by minimizing surface-related quenching effects and separating the Nd^{3+} ions from the activators in the core, as already reported for other core–shell UCNPs.[50–56]

It was possible to control the crystalline phase and size of the nanoparticles (NPs) by varying the time and temperature of the reaction (see below). The temperature and time regimes explored as part of this work allowed us to prepare UCNPs with sizes between 5 and 30 nm. To note, size and phase formation were unaffected by the concentration of the dopants ($Nd^{3+}/Yb^{3+}/Er^{3+}$) used during the synthesis. However, as mentioned before, our interest was in delivering sub-10 nm pure-phase NPs. For this reason, the discussion in this manuscript will be primarily confined to sub-10 nm particles, and UCNPs of other sizes, if discussed, will only be for comparison purposes. The preparation conditions of the UCNPs discussed in this work are summarized in Table 1. The as-synthesized UCNPs were easily dispersible in different nonpolar solvents, such as *n*-hexane, cyclohexane, and chloroform.

Transmission electron microscopy (TEM) was used to obtain the size distribution of the UCNPs. The TEM images show monodisperse particles with uniform spherical morphology (Figure 1 and Table 2). Statistical analyses revealed narrow particle-size distributions for both the core [sample A: (9 ± 1) nm] and core–shell particles [sample C: (11 ± 1) nm]. Consequently, growing a shell around the core particles resulted in a size increase by about 2 nm. Larger particles were obtained with extended reaction times, and they remained monodisperse with a spherical shape [sample B: (20 ± 2) nm, Figure S2]. Dynamic light scattering (DLS) measurements in *n*-hexane further corroborated the narrow size distributions of the particles [sample A: (9 ± 3) nm, sample B: (23 ± 6) nm, sample C: (12 ± 3) nm; Table 2 and Figure S3].

Table 1. Reaction conditions used for the preparation of UCNP samples discussed in this work.

Sample[a]	Composition	Solvent	Time [min]	Temperature [°C]
A	$NaYF_4$: $Nd^{3+}/Yb^{3+}/Er^{3+}$ (1/20/2%): core	T66/OA (3:2, *v*/*v*)	10	319
B	$NaYF_4$: $Nd^{3+}/Yb^{3+}/Er^{3+}$ (1/20/2%): core	T66/OA (3:2, *v*/*v*)	60	320
	$NaYF_4$: Nd^{3+}/Yb^{3+} (25/10%): shell		5[a]	305
C	$NaYF_4$: $Nd^{3+}/Yb^{3+}/Er^{3+}$ (1/20/2%): core	T66/OA (3:2, *v*/*v*)	10	319
	$NaYF_4$: Nd^{3+}/Yb^{3+} (25/10%): shell		5[b]	305
D	$NaYF_4$: $Nd^{3+}/Yb^{3+}/Er^{3+}$ (1/20/2%): core	T66 (neat)	10	303
E[c]	$NaYF_4$: Yb^{3+}/Er^{3+} (20/2%): core	T66/OA (3:2, *v*/*v*)	10	319

[a] Samples A–C and E were pure hexagonal (β-phase), whereas sample D crystallized in the cubic α-phase (refer to XRD analysis for more details). [b] Shell precursor solution was added over 30 min at 305 °C. [c] Crystalline phase and size distribution were obtained from the powder XRD and DLS data, respectively (Figure S3).

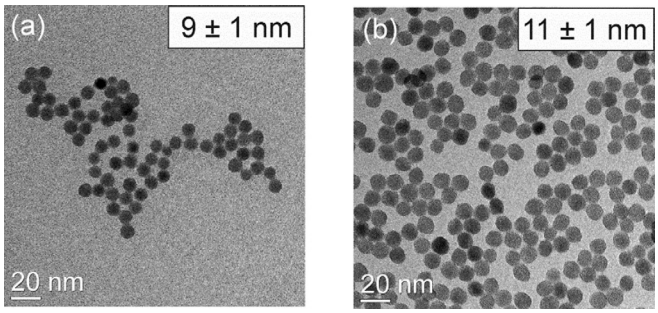

Figure 1. Bright-field TEM images of a) sample A [$NaYF_4$:Nd^{3+}/Yb^{3+}/Er^{3+} (1/20/2%), core] and b) sample C [$NaYF_4$:Nd^{3+}/Yb^{3+}/Er^{3+} (1/20/2%) @ $NaYF_4$:Nd^{3+}/Yb^{3+} (25/10%), core–shell]. The relative ratio of dopants in the NPs is given as mol%, as obtained by inductively coupled plasma mass spectrometry analysis.

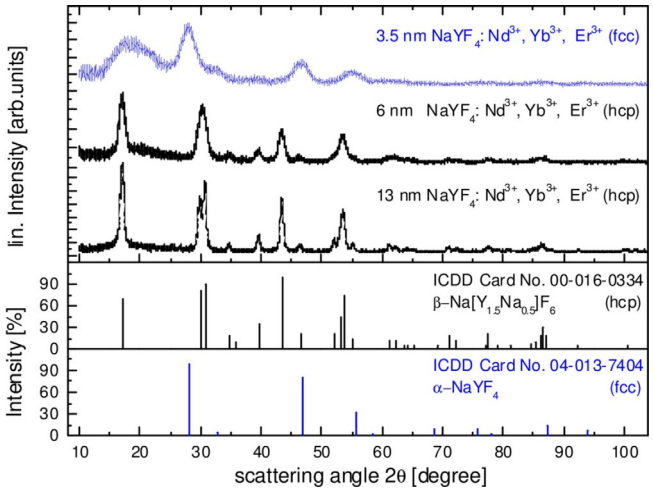

Figure 2. X-ray powder diffractograms of synthesized phase-pure UCNPs: sub-10 nm cubic (sample D, crystallite size: ca. 3.5 nm) and hexagonal (sample A, crystallite size: ca. 6 nm) UCNPs doped with Nd^{3+}/Yb^{3+}/Er^{3+} along with the non-doped hcp (β) and cubic (α) reference bulk materials. The diffractogram for the over-10 nm hexagonal UCNPs (sample B, crystallite size: ca. 13 nm) is provided for comparison. The mentioned crystallite sizes were obtained from the recorded diffractograms by using the Williamson–Hall equation [Eq. (1)].

Table 2. Comparison of various size-distribution metrologies used for representative samples of sub-10 nm (sample A) and over-10 nm (sample B) hexagonal phase UCNPs.[a]

Sample	Size distribution [nm]			
	TEM	XRD	DLS (*n*-hexane)	SAXS (*n*-hexane)
A	9±1	6±1	9±3	8.8±0.5
B	20±2	13±1	23±6	22±2

[a] Sample A: [$NaYF_4$:Nd^{3+}/Yb^{3+}/Er^{3+} (1/20/2%), core]; sample B: [$NaYF_4$:Nd^{3+}/Yb^{3+}/Er^{3+} (1/20/2%)@$NaYF_4$:Nd^{3+}/Yb^{3+} (25/10%), core–shell].

Phase and corresponding lattice-parameter determination were performed by using X-ray powder diffraction (XRD) analysis. In addition, by using the Williamson–Hall equation [Eq. (1) in the Experimental Section, X-ray diffraction studies], we also determined the average coherent crystallite sizes from the recorded diffractograms (see below). Here, the recorded XRD patterns (Figure 2) indicate that (Yb^{3+}/Er^{3+}/Nd^{3+})-doped $NaYF_4$ nanoparticles (NPs) crystallized either in the cubic face-centered cubic (fcc) α-phase (space group: $Fm\bar{3}m$) or in the hexagonal β-phase (space group: $P63/m$).[17,57] The 3.5 nm sized $NaYF_4$ particles (prepared in pure T66) crystallized in the fcc α-phase [ICDD(2016) card No. 04–013–7404],[58] whereas 6 and 13 nm sized particles (prepared in OA/T66 mixtures) grew in the hcp β-phase [ICDD(2016) card No. 00–16–0334].[59] On the other hand, small single hexagonal-phased (hcp) particles could be readily produced by performing the reaction in a binary solvent mixture of T66/OA (3:2, *v*/*v*) and by raising the reaction temperature to 317 °C or above. The lattice constants of the 3.5 nm sized fcc UCNPs were slightly higher than the reference data from the ICDD cards with $a = 5.54$ Å [ICDD (2016) card No. 04–013–7404: $a = 5.47$ Å]. Similar behavior was found for the hexagonal particles with $a = 6.01$ Å and $c = 3.53$ Å [ICDD (2016) card No. 00–16–0334: $a = 5.96$ Å, $c = 3.53$ Å].[15,59]

It should be emphasized that upon using T66 as a co-solvent, a reaction time as short as 10 min (at 319 °C) was sufficient to produce sub-10 nm pure hexagonal (β-phase) UCNPs. In comparison, most of the reported thermal decomposition methods employing different solvent combinations generally need longer reaction times or additional ions (e.g. Li^+, Ca^{2+}, Mn^{2+}, Gd^{3+}) to trigger the phase transformation and to produce small-sized hexagonal crystals.[14,25,27–33,47,57,60–62]

Here, one should note that although the calculation method based on Equation (1) has its limitations, for particles with an average size of the order of 10 nm and below, the calculated uncertainty was estimated to be about 1 nm and slightly increases with decreasing particle size. Consequently, a comparison with dynamic light scattering (DLS detects the hydrodynamic radius of a particle in solution), with TEM, or with small-angle X-ray scattering (SAXS) analysis leads to a particle size that always has to be larger than the corresponding crystallite size determined by XRD (Table 2). A possible reason for small particles is the strong influence of the surface and for larger particles is that during particle growth single-crystallite UCNPs are not always formed.

We also used the SAXS method to validate the particle-size distributions. SAXS is a promising technique for measuring particle sizes below 10 nm, a point at which other methods may reach their detection limit. It is sensitive to scattering density variations and was used here to analyze the shape and the size of the synthesized UCNPs. With SAXS, however, it is not possible to measure the contributions of individual atoms to the scattering signal but rather the changes in scattering contrast.[63] The measurements were performed by using a solution of NPs in *n*-hexane (Figure 3). Therefore, the scattering contrast was formed by changes between the NPs and the solvent. Additionally, we assumed that there was negligible spatial correlation between the individual particles in solution and that the resulting scattering signal was the averaged sum of the scattering signal of one single mean particle. A major advantage of this technique exists in the possibility to observe NP shapes

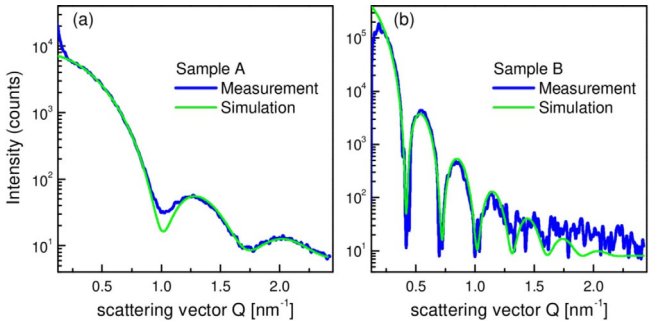

Figure 3. Integrated SAXS signals of a) sub-10 nm sample A [$NaYF_4$:Nd^{3+}/Yb^{3+}/Er^{3+} (1/20/2%), core] and b) over-10 nm sample B [$NaYF_4$:Nd^{3+}/Yb^{3+}/Er^{3+} (1/20/2%)@$NaYF_4$:Nd^{3+}/Yb^{3+} (25/10%), core–shell]. The measurements were performed on NP solution in hexane. The model was simulated and fitted to the measurements by assuming a filled nanoparticle in solution, allowing certain size variation.

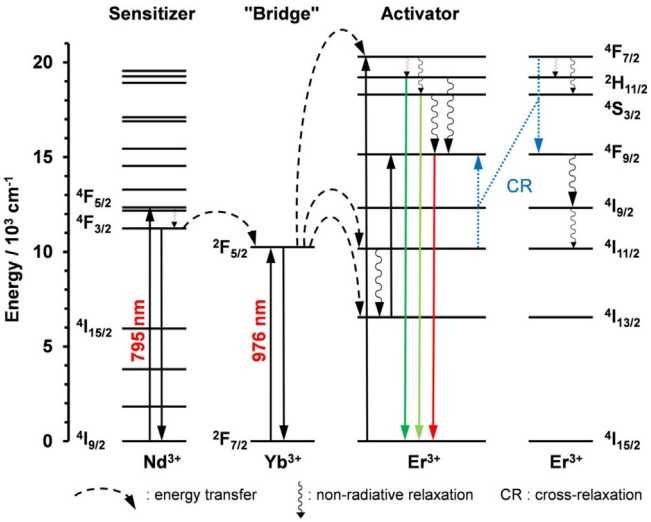

Scheme 1. Schematic representation of the energy levels involved in the UC mechanism of a Yb^{3+} and Er^{3+} dopant ion system following excitation at $\lambda = 976$ nm. Furthermore, the UC mechanism of a Nd^{3+}, Yb^{3+}, and Er^{3+} dopant ion system following excitation at $\lambda = 795$ nm is shown. The solid lines pointing upwards represent energy absorption, the dashed lines represent energy-transfer processes, the wavy lines represent nonradiative relaxation processes, the blue dotted lines represent cross-relaxation (CR) processes between excited Er^{3+} species, and the solid lines pointing downwards represent visible and NIR emissions. The excitation energy transfer from Yb^{3+} ions to Er^{3+} ions occurs by long-range energy migrations from the Yb^{3+} absorption site through the Yb sublattice.[67]

and sizes in situ, without any sample preparation-induced effects.

The program "X+"[64] was used to analyze the radially integrated scattering pattern by assuming a model that represents the UCNPs as filled spheres of known density. The sphere radius was used as a single fitting parameter. In our case, the values obtained from this readily available method matched very well with the TEM and DLS results and even extended our knowledge of NP shape.

2.2. Upconversion Luminescence Properties

2.2.1. Analysis of Di-doped (Yb^{3+}/Er^{3+}) β-$NaYF_4$ UCNPs

The upconversion luminescence spectrum of β-phase $UCNP_{core}$ (β-$NaYF_4$:Yb^{3+}/Er^{3+} 20/2%) measured in cyclohexane shows three intense bands centered at $\lambda = 525$ ($^2H_{11/2} \rightarrow {}^4I_{15/2}$ transition, G1), 545 ($^4S_{3/2} \rightarrow {}^4I_{15/2}$ transition, G2), and 660 nm ($^4F_{9/2} \rightarrow {}^4I_{15/2}$ transition, R), upon excitation at $\lambda = 976$ nm, consistent with excitation energy-transfer (ET) processes between the Yb^{3+} (sensitizer) and Er^{3+} (activator) ions (Scheme 1).[35–37,65,66]

An increase in the UC emission intensity was observed upon increasing the size of the particles (Figure 4). Furthermore, the relative G_{G1+G2}/R peak ratio of $UCNP_{core}$ also decreased upon increasing the NP diameter. These effects can be attributed to a decrease in the surface-area-to-volume ratio and subsequent reduction in the contributions from surface-related luminescence quenching processes, resulting in a higher UC emission intensity (Figure 5). As a consequence, the excited-state lifetime of the Er^{3+} ions increased, which caused the probability for cross-relaxation processes between two excited Er^{3+} ions to increase as well. This resulted in further population of the $^4F_{9/2}$ energy level of the Er^{3+} ions, which thereby enhanced the luminescence intensity of the $^4F_{9/2} \rightarrow {}^4I_{15/2}$ transition (R). This effect was independent of the particle shape, as the surface-area-to-volume ratio (calculated by assuming UCNPs as spheres or as hexagonal prisms) showed similar trends.[68]

The UC luminescence properties of $UCNP_{core}$ β-$NaYF_4$:Yb^{3+}/Er^{3+} (20/2%) covered with an inert shell of pure $NaYF_4$

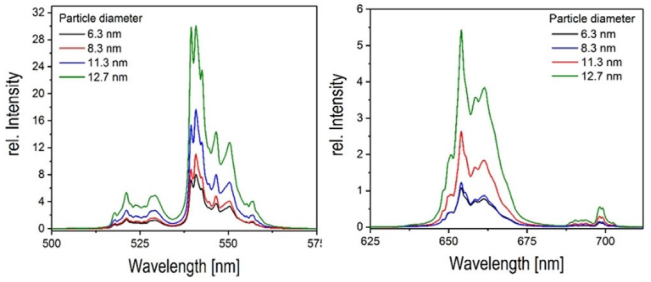

Figure 4. Comparison of the UC emission intensities of $UCNP_{core}$ β-$NaYF_4$:Yb^{3+}/Er^{3+} (20/2%) UCNPs with different sizes, measured in cyclohexane, upon excitation at $\lambda = 976$ nm. The Er^{3+} emission bands G1 and G2 (left) as well as R (right) are shown.

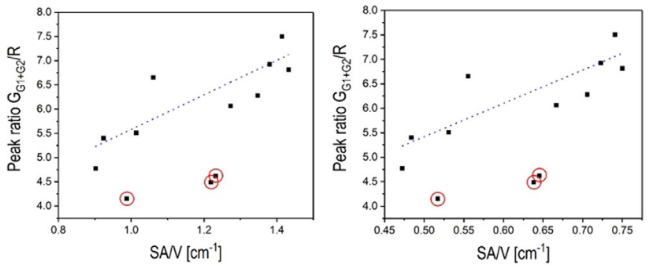

Figure 5. The G_{G1+G2}/R peak ratio of the UC emission bands of $UCNP_{core}$ β-$NaYF_4$:Yb^{3+}/Er^{3+} (20/2%) as a function of the surface area to volume (SA/V) ratio assuming a particle shape of hexagonal prism (left) and sphere (right). The red circles mark $UCNP_{core}$ covered with a nonactive shell of pure $NaYF_4$ ($UCNP_{core}$@$NaYF_4$).

($UCNP_{core}$@$NaYF_4$) were also evaluated. Typically, the vibrational coupling interaction between the solvent (or ligand) and the lanthanide ions results in a decrease in the UC emission. This coupling is much more effective for the $^2F_{5/2}$ level of the Yb^{3+} ions or the $^4I_{11/2}$ and $^4I_{13/2}$ levels of the Er^{3+} ions, which are crucial for the population mechanism of the state responsible for the UC emission ($^4F_{9/2}$, $^2H_{11/2}$, or $^4S_{3/2}$). In contrast, the probability of vibrational coupling involving $^4F_{9/2}$, $^2H_{11/2}$, or $^4S_{3/2}$ levels of Er^{3+} is much lower because of the higher number of phonons needed.[69] Shielding the sensitizer ions in the core is thus necessary for reducing this vibrational coupling. Moreover, the growth of a shell around the core of the UCNPs also serves to passivate trap states due to lattice defects on the surface.

The core–shell UCNPs displayed higher UC emission than the $UCNP_{core}$ materials (Figure 6). Passivation of the UCNP surface with a 1 nm thick shell led to a roughly twofold increase in the UC luminescence intensity (this increase was also corroborated by an increase in the luminescence decay times, see below), providing evidence for surface-related quenching effects. Moreover, the R transition increased its intensity as a result of the presence of the shell, which thus caused the G_{G1+G2}/R peak ratio of $UCNP_{core}$@$NaYF_4$ to be much lower than that of $UCNP_{core}$ of the same size (Figure 5, points circled in red).

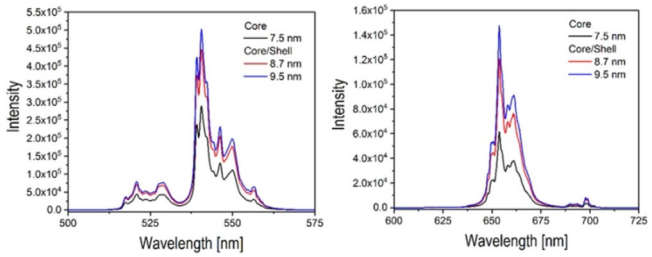

Figure 6. Influence of the shell thickness on the UC emission intensity of $UCNP_{core}$@$NaYF_4$ (in cyclohexane) excited at $\lambda = 976$ nm. Er^{3+} transitions G1 and G2 (left) as well as R (right) are shown. The luminescence of core-only β-$NaYF_4$:Yb^{3+}/Er^{3+} (20/2 %) UCNPs is shown for comparison (black solid trace).

We also studied the luminescence decay kinetics of the G1, G2, and R transitions for the UCNPs. Both the $UCNP_{core}$ and $UCNP_{core}$@$NaYF_4$ particles exhibited luminescence decay times on the microsecond timescale (Table 3). For data analysis of $UCNP_{core}$, a biexponential decay law was used [see Eqs. (2) and (3) in the Experimental Section, Luminescence Spectroscopy]. The complex decay kinetics[70] can be attributed to the presence of two different populations of erbium ions: the former is located inside the NP (τ_2, bulk phase) and the latter (τ_1) lies on the surface of the UCNPs. The R band showed a longer average decay time ($\tau_m = 67$ μs) than the pooled green emission band (G_{G1+G2}, $\tau_m = 55$ μs) [see Eq. (4) in the Experimental Section, Luminescence Spectroscopy]. Furthermore, an increase in the kinetics of UC luminescence was observed, and the rise kinetics were fivefold longer for R than for G_{G1+G2}. The difference in rise times resulted from the different population kinetics and rate constants of the involved energy levels.

Table 3. Upconversion decay kinetics of the pooled green emission G_{G1+G2} and red emission R of $UCNP_{core}$ and $UCNP_{core}$@$NaYF_4$ ($\lambda_{ex} = 976$ nm).

Sample	Emission	Rise [μs]	τ_m [μs]
$UCNP_{core}$	G_{G1+G2}	1.7	54.9
	R	10.7	66.7
$UCNP_{core}$@$NaYF_4$	G_{G1+G2}	7.1	75.0
	R	20.5	90.4

For $UCNP_{core}$@$NaYF_4$, an increase in the UC luminescence decay time was registered, which indicated a lower contribution from nonradiative deactivation processes. For $UCNP_{core}$@$NaYF_4$, no Er^{3+}-based surface species were expected to contribute to the overall luminescence. As a result, monoexponential UC decay kinetics were observed (see Figure S5). Furthermore, the presence of the inert shell had a distinct effect of increasing the rise kinetics (Table 3). This was due to the fact that the $NaYF_4$ inert shell prevented nonradiative deactivation of Yb^{3+} and Er^{3+} excited states caused by ligand and/or cyclohexane CH oscillators.[71] Under these conditions, the excitation energy was dissipated by means of long-distance migrations through the Yb sublattice and was finally transferred to Er^{3+}, which resulted in longer rise times than those observed for $UCNP_{core}$.[72]

2.2.2. Analysis of Tri-doped (Yb^{3+}/Er^{3+}/Nd^{3+}) β-$NaYF_4$ UCNPs

The UC properties of tri-doped UCNPs containing Nd^{3+} ions as a primary sensitizer, Yb^{3+} as bridging ions (secondary sensitizer), and Er^{3+} as activator ions were also investigated. Here, the Nd^{3+} ions first absorb photons in the NIR range ($\lambda_{ex} = 795$ nm, $^4I_{9/2} \rightarrow {}^4F_{5/2}$ transition), and this is followed by relaxation to the $^4F_{3/2}$ level. Next, an ET process sensitizes the bridging Yb^{3+} ions [$^4F_{3/2}$ (Nd^{3+}) + $^2F_{7/2}$ (Yb^{3+}) → $^4I_{9/2}$ (Nd^{3+}) + $^2F_{5/2}$ (Yb^{3+})], which in turn transfer the excitation energy to the $^4I_{11/2}$ state of Er^{3+}, followed by the UC processes described in Scheme 1. Moreover, direct excitation of the Yb^{3+} ions at $\lambda = 976$ nm is also possible in these systems, obviating the participation of Nd^{3+} ions in the ET chain.

Under $\lambda = 976$ nm excitation, upon increasing the Nd^{3+} doping level from 1 to 5 % in $UCNP_{core,Nd}$, a significant decrease in the UC emission intensity was observed (Figure 7, left). One explanation for the observed change in UC emission is that as

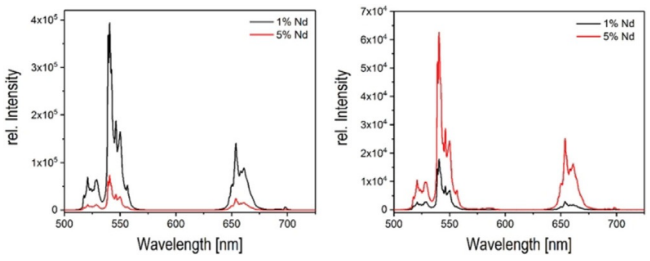

Figure 7. Upconversion emission spectra of $UCNP_{core,Nd}$ (in cyclohexane) doped with 1 and 5 % Nd^{3+} upon excitation at $\lambda_{ex} = 976$ nm (left) and 795 nm (right). Size of UCNPs: (9 ± 1) nm.

the concentration of Nd^{3+} ions was increased, the probability of parasitic energy back-transfer processes between the Er^{3+} and Nd^{3+} ions increases, which results in lower UC emissions.[73] In contrast, under excitation at $\lambda = 795$ nm, an enhancement in the UC luminescence was observed as Nd^{3+} doping was increased (Figure 7, right). These results can be ascribed to the different roles of the Nd^{3+} ions in the two UC processes. At $\lambda_{ex} = 976$ nm, the Nd^{3+} ions only act as quenchers for the excited Er^{3+} ions, whereas if the UCNPs are excited at $\lambda = 795$ nm, the Nd^{3+} ions act as primary sensitizers and absorb light directly. Moreover, the absorption cross section of Nd^{3+} is 10-fold higher at $\lambda_{ex} = 795$ nm than that of Er^{3+} at $\lambda = 976$ nm,[74] which is also beneficial to the efficiency of the UC process.

Quantitative evaluation of the relative UC emission intensities upon excitation at $\lambda = 795$ and 976 nm was also performed by using $UCNP_{core,Nd}$ (1% Nd^{3+} doping). As can be observed from Figure 8 (left), the $UCNP_{core,Nd}$ emission intensity at $\lambda = 795$ nm was only 6% of the corresponding UC emission intensity at $\lambda = 976$ nm excitation. Lowering of the UC intensity can be rationalized on the basis of an additional energy transfer step involving the Nd^{3+} and Yb^{3+} ions that occurs under $\lambda = 795$ nm excitation, which is anticipated to decrease the efficiency of the entire ET chain. Covering the $UCNP_{core,Nd}$ with an active $NaYF_4$:Nd^{3+}/Yb^{3+} (25/10%) shell, however, significantly enhanced the UC emission intensity at both excitation wavelengths (Figure 8, right). UC emission intensity at $\lambda_{ex} = 795$ nm was calculated to be 47% of its UC emission upon excitation at $\lambda = 976$ nm, which reaffirmed the ability of the active shell to reduce Er^{3+}–Nd^{3+} energy back transfer as a consequence of the spatial separation between these two ions.[73]

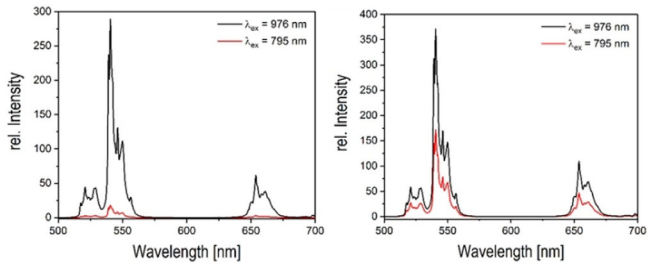

Figure 8. Upconversion emission spectra of $UCNP_{core,Nd}$ (left, sample A) and $UCNP_{core,Nd}$@$NaYF_4$:Nd^{3+}/Yb^{3+} (25/10%) (right, sample C) upon excitation at $\lambda = 976$ and 795 nm [power density (ϕ) = 85 mW cm^{-2} for both excitation wavelengths; $c_{UCNP} = 7$ mg mL^{-1} in cyclohexane].

The luminescence decay kinetics of the G1, G2, and R transitions of the $UCNP_{core,Nd}$ and $UCNP_{core,Nd}$@$NaYF_4$:Nd^{3+}/Yb^{3+} (25/10%) particles were studied under excitation at $\lambda = 795$ and 976 nm (Table 4). Data analysis revealed that core–shell $UCNP_{core,Nd}$@$NaYF_4$:Nd^{3+}/Yb^{3+} (25/10%) exhibited longer decay times than $UCNP_{core,Nd}$. In addition, the rise times for all UC transitions were longer, which suggested an efficient long-range energy migration took place between the sensitizer ions in the shell and the activator ions in the core,[72] as already described for $UCNP_{core}$ and $UCNP_{core}$@$NaYF_4$. Overall, these results underline the minor contribution of nonradiative deactivation processes in core–shell UCNPs. Moreover, at $\lambda_{ex} = 795$ nm, the Nd^{3+} ions in the shell, present in a relatively high concentration, acted as harvesting units and further improved the brightness of UCNP as a result of increased absorption per NP.

Table 4. Upconversion decay kinetics of the pooled green emission G_{G1+G2} and red emission R of $UCNP_{core,Nd}$ and $UCNP_{core,Nd}$@$NaYF_4$: Nd^{3+}/Yb^{3+} (25/10%) particles.

Sample	Emission	Rise [μs] $\lambda_{ex} = 795$ nm	τ_m [μs] $\lambda_{ex} = 795$ nm	Rise [μs] $\lambda_{ex} = 976$ nm	τ_m [μs] $\lambda_{ex} = 976$ nm
$UCNP_{core,Nd}$	G_{G1+G2}	4.3	50.7	1.7	54.9
	R	13.2	70.2	10.7	66.7
$UCNP_{core,Nd}$@$NaYF_4$:Nd^{3+}/Yb^{3+} (25/10%)	G_{G1+G2}	20.5	73.8	7.1	75.0
	R	39.7	113.2	20.5	90.4

Insight into the nature of the upconversion mechanism was obtained by analyzing the variation in integrated intensities of the green (G1 and G2) and red (R) emission bands as a function of applied excitation power density (ϕ). The results showed that in $UCNP_{core,Nd}$, the G1 and G2 transitions were based on a two-photon process at $\lambda_{ex} = 976$ nm (Figure S5). The R transition, on the other hand, could be described as a two-photon process as well as a three-photon process. The $UCNP_{core,Nd}$@$NaYF_4$:Nd^{3+}/Yb^{3+} (25/10%) particles behaved similar to the $UCNP_{core,Nd}$ particles. There was no significant increase in the number of photons (n), and the addition of Nd^{3+} (25 mol%) and Yb^{3+} (10 mol%) in the shell had no further influence on the UC population processes. Moreover, no variations in n for the G1 and G2 transitions upon excitation at $\lambda = 795$ nm (Figure S6) in either the core or core–shell UCNPs were registered. However, a decreased probability of three-photon processes was observed for R transitions in $UCNP_{core,Nd}$@$NaYF_4$:Nd^{3+}/Yb^{3+} (25/10%), which can be attributed to a significant change in the favored population mechanism for R transition due to changes in population density of the excited Er^{3+} levels.

The comparison between excitation wavelength did not show large differences in the number of photons [e.g. $n = 1.8$ ($\lambda_{ex} = 795$ nm) and $n = 1.9$ ($\lambda_{ex} = 976$ nm) for the $^4S_{3/2} \rightarrow {}^4I_{15/2}$ transition]. This is in contrast to recent findings by Skripka et al.,[75] who described larger differences for n (e.g. for the $^4S_{3/2} \rightarrow {}^4I_{15/2}$ transition, a reported decrease from $n = 1.98$ at $\lambda_{ex} = 976$ nm to $n = 1.24$ at $\lambda_{ex} = 806$ nm). It should be underlined that the excitation conditions used in these two works are very different. Whereas Skripka et al. reported on results for excitation power density (ϕ) > 10 W cm^{-2} under continuous-wave excitation, we used smaller ϕ (< 200 mW cm^{-2}) under pulsed excitation. Thus, in our case, direct excitation of Er^{3+} by ground state absorption (GSA) or excited state absorption (ESA) processes, which would lead to a decrease in n, was minimal, and the observed n values for both excitation wavelengths do not differ significantly. Additionally, the UCNPs investigated in the present study are smaller in size and endowed with a thinner shell, resulting in different contributions from surface-related processes due to a different surface-area-to-volume ratio.

At both excitation wavelengths, the intensity ratio G1/G2 was constant for the investigated range of excitation power densities (13–85 mW cm^{-2}) for the core and core–shell NPs (Figure 9). The G/R ratio, on the other hand, showed a significant decrease at higher ϕ values upon excitation at $\lambda =$ 976 nm. This indicated a higher probability of cross-relaxation processes involving Er^{3+} ions, which resulted in a higher population of the $^4F_{9/2}$ level responsible for the red emission. This effect was independent of the architecture of the particles (core or core–shell UCNPs).

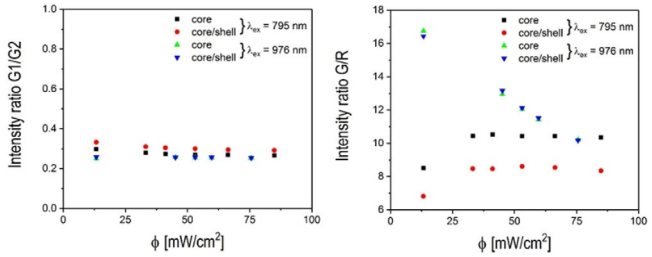

Figure 9. Plot of the UC emission intensity ratio G1/G2 (left) and G/R (right) of $UCNP_{core,Nd}$ and $UCNP_{core,Nd}$@$NaYF_4$:Nd^{3+}/Yb^{3+} (25/10%) as a function of the excitation power density (ϕ) measured for $\lambda_{ex} =$ 976 and 795 nm.

In contrast, the power density dependency of the G/R ratio was no longer observed if the UCNPs were excited at $\lambda =$ 795 nm (Figure 9, right). This behavior can be explained on the basis of the influence of the Nd^{3+} ions on the saturation effect in the ET chain. Nd^{3+} ions with their large absorption cross section (1.2×10^{-19} cm^2 at $\lambda =$ 808 nm[74] vs. 1.2×10^{-20} cm^2 for Yb^{3+} ions at $\lambda =$ 980 nm) possibly lower the saturation intensity (which is inversely proportional to the cross section)[76] by about one order of magnitude, and this leads to a constant G/R ratio under the conditions of our study.

Despite the more efficient light-absorption ability, the G/R transition band ratio of $UCNP_{core,Nd}$@$NaYF_4$:Nd^{3+}/Yb^{3+} (25/10%) was lower than that calculated for $UCNP_{core,Nd}$ because of the higher rate of Er^{3+}-based cross-relaxation processes, which are favored in the presence of Nd^{3+} ions. Notably, variation in the intensity ratio of the UC emissions bands was found to be highly dependent on the lanthanide ions used and the composition of the host lattice. For instance, the excitation power density did not have any effect on the G/R ratio of Er^{3+}-doped α-phase $NaYF_4$ UCNPs (data not shown). Nevertheless, the excitation power density could have a huge impact on the ratio of emission bands and should always be taken into careful consideration upon understanding the UC luminescence properties of UCNPs.

3. Conclusions

We demonstrated a facile method for the preparation of high-quality sub-10 nm β-phase $NaYF_4$ nanocrystals by introducing Therminol® 66 as a new reaction co-solvent. The size and morphology of upconverting nanoparticles (UCNPs) could be precisely tuned to the 1–10 mmol reaction scale by using short reaction times and by varying the reaction temperature. Using this protocol, sub-10 nm Nd^{3+}/Yb^{3+}/Er^{3+} tri-doped core and related core–shell β-$NaYF_4$ UCNPs were also synthesized. These UCNPs showed efficient upconversion (UC) luminescence intensity under irradiation at an intrinsically biocompatible wavelength of 795 nm. The advantage of having different options (e.g. having two sensitizer ions present in the UCNPs) to sensitize the UC luminescence was demonstrated. In general, we presented a highly time-saving method for the synthesis of sub-10 nm UCNPs with improved luminescence properties that hold great potential for various biomedical applications. The ability to extend the synthetic methodology to the design of core–shell UCNPs with a shell thickness of at least 1 nm highlights the versatility of the reported protocol. Our future research will focus on understanding the exact role of Therminol® 66 in the growth mechanism of the UCNPs and unraveling the mechanisms underlying the involved phase-transition processes. To expand greatly the applicability of this method in the synthesis of highly luminescent ultrasmall UCNPs, we are also exploring its use for readily delivering nanoparticles with other lanthanide and host matrix compositions.

Experimental Section

Chemicals

Yttrium(III) chloride hexahydrate (99.99%), ytterbium(III) chloride hexahydrate (99.99%), neodymium(III) chloride hexahydrate (99.99%), erbium(III) chloride hexahydrate (99.99%), ammonium fluoride (ACS reagent ≥98.0%), sodium hydroxide (reagent grade ≥98.0%), and oleic acid (technical grade 90%) were purchased from Sigma–Aldrich and were used as received. Therminol® 66 (T66) was supplied by JULABO GmbH (Seelbach, Germany, product number: 8940131). All other organic solvents used were of the highest grade available.

Synthesis

Sodium oleate: Oleic acid (OA, 50 mmol) was added dropwise to a solution of sodium hydroxide (50 mmol) in absolute ethanol (700 mL). The mixture was stirred overnight at RT. Sodium oleate was obtained as a white solid after evaporation of the solvent under reduced pressure at 40 °C.

Core UCNPs ($UCNP_{core,Nd}$): In a typical procedure, YCl_3 (0.77 mmol), $NdCl_3$ (0.01 mmol), $YbCl_3$ (0.2 mmol), and $ErCl_3$ (0.02 mmol) were dissolved in a mixture of T66/OA (3:2, *v/v*, 20 mL), and the mixture was degassed for 45 min at 120 °C under vacuum to obtain a yellow homogenous solution. Following this, the solution was cooled to 90 °C. Afterwards, sodium oleate (2.5 mmol) and ammonium fluoride (4 mmol) were added at once under an argon atmosphere. A second degassing step at 90 °C was then performed to generate anhydrous, oxygen-free conditions without premature decomposition of NH_4F. Subsequently, the solution was heated (heat rate 10 °C min^{-1}) up to a final temperature of 280–325 °C (±1 °C). The mixture was maintained at this temperature for 10–60 min under an argon atmosphere and was then cooled rapidly by a strong stream of air to give particles with a defined size (Table 1). After cooling, the UCNPs were precipitated from the solution by the addition of absolute ethanol (25 mL) and were isolated by centrifugation (3939×g, 5 min). The supernatant was discarded,

and the white pellet was washed several times by dispersing it in a minimal amount of *n*-hexane. The nanoparticles were then precipitated again with the addition of ethanol and were centrifuged. This washing procedure was performed to ensure elimination of the reaction surfactants as well as any NaF impurities that were formed. Finally, the purified oleate-coated UCNPs were dispersed in *n*-hexane or chloroform (10 mL). The UCNPs could be stored at room temperature and were colloidally stable for several months. The molar compositions of lanthanide ions in the final UCNP samples were determined by inductively coupled plasma mass spectrometry (ICP-MS) and showed good agreement with the stoichiometric ratios used for the synthesis.

Core–shell UCNPs ($UCNP_{core,Nd}$@$NaYF_4$:Nd^{3+}/Yb^{3+} 25/10%): A shell precursor solution was prepared as follows: T66 (8 mL), OA (4 mL), YCl_3 (0.65 mmol), $NdCl_3$ (0.25 mmol), and $YbCl_3$ (0.1 mmol) were mixed in a 50 mL flask, and the mixture was heated at 120 °C for 60 min under vacuum. Afterwards, the solution was cooled to 90 °C. Next, NH_4F (4 mmol) and sodium oleate (2.5 mmol) were added under an argon atmosphere. The mixture was stirred for another 30 min under an argon atmosphere to dissolve the solids. Finally, the shell solution was stored at RT until further use.

To apply a shell on the synthesized core nanoparticles, the slow injection method was used. First, a solution of core UCNPs (60 mg) in T66/OA (3:2, *v/v*, 20 mL) was heated at 75 °C for 30 min. Afterwards, an argon atmosphere was applied, and the temperature was elevated to the injection temperature of 305 °C. Thereafter, the shell precursor (1 mL) solution was added dropwise while controlling the injection velocity (2 mL h^{-1}) by using a syringe pump. After the addition of the precursor solution, the temperature was maintained at 305 °C for 5 min before it was cooled to 75 °C. The purification steps were the same as those described for the core UCNPs. The molar compositions of the lanthanide ions in the final UCNP samples were determined by ICP-MS and showed good agreement with the stoichiometric ratios used for the synthesis.

TEM

Bright-field TEM analysis was performed by using an image C_s-corrected FEI Titan 80–300 electron microscope operating at an accelerating voltage of 300 kV. The size distributions of the UCNPs were determined from the acquired TEM images by using ImageJ image-processing software, by analyzing 300 particles in each case (version 1.50b, NIH, USA).

DLS Measurements

The hydrodynamic diameters of the prepared nanocrystals were determined by DLS by using a Malvern Zetasizer Nano ZS Instrument with a He–Ne laser ($\lambda = 632$ nm) (Malvern Instruments GmbH, Germany). Measurements were performed at a constant temperature of 25 °C with a detection angle of 173° and were processed by means of the associated Zetasizer software version 7.12.

XRD Studies

The crystal structures and phase purities of the prepared nanomaterials were studied by powder XRD measurements by using an Empyrean diffractometer from PANalytical equipped with a Göbel mirror using CuKα radiation ($\lambda = 0.154$ nm). The XRD patterns were recorded by a PIXcel3D 2×2 detector in the 2θ range of 1.3 to 130.1° by using a typical scanning step of 0.013° per 592 s. For XRD analysis, hydrophobic nanoparticle samples (dissolved in *n*-hexane) were precipitated in an excess amount of ethanol, and a thick film of a concentrated solution was slowly dried on a silicon wafer.

The crystallite size (L) was calculated from the X-ray diffractograms by using the Williamson–Hall equation [Eq. (1)]:

$$\Delta q(q) = k \bullet \frac{2\pi}{L} + \varepsilon' \bullet q; q = \frac{4\pi}{\lambda} \bullet sin\ \theta \qquad (1)$$

in which L is the coherent size of the crystallite, k is a shape factor depending on particle morphology (here, 0.9 was used), λ is the X-ray wavelength, ε' is an equivalent to the microstrain in the crystallite itself or corresponds to lattice constant variations of an infinite number of crystallites, θ is the Bragg angle of the X-ray diffraction peak, and Δq is the full width at half maximum of the diffraction peaks as a function of q. The reciprocal of the intercept Δq_0 ($L = 2k\pi/\Delta q_0$) yielded the average crystallite size, L. The values given in Table 2 are the average crystallite sizes based on all isolated peaks calculated for samples A and B.[77]

SAXS Studies

SAXS measurements were performed on UCNP solutions in *n*-hexane by using a modified Empyrean diffractometer equipped with a two-dimensional side-by-side optics and an extended fine-focus Cu tube with a point spot size of 150 µm. It was ensured that the primary beam width remained almost constant over the entire dynamic range and that no secondary maxima occurred. We used a PIXcel3D 2×2 detector to register the scattering signal. The setup allowed us to work without any beam stop; the detector distance was varied between 155 and 500 mm depending on the size of the nanoparticles. Typical measurement times for one SAXS measurement were about 5000 s.

Luminescence Spectroscopy

Steady-state as well as time-resolved upconversion luminescence spectra were obtained by applying a wavelength tunable pulsed Nd:YAG/OPO laser system (laser: Quanta Ray, Spectra-Physics, Mountain View, CA, USA; OPO: GWU-Lasertechnik Vertriebsges. GmbH, Erftstadt, Germany) operating at 10 Hz as the excitation light source (at 26 mJ, 120 mW cm^{-2}) and were recorded by using an intensified CCD camera (iStar DH720-18V-73, Andor Technology, Belfast, Great Britain) coupled to a spectrograph (Shamrock SR 303i, Andor Technology, Belfast, Great Britain) equipped with a 600 lines per mm grating blazed at 500 nm. The luminescence measurements were collected in the so-called boxcar technique by applying an initial gate delay of $\Delta t = 500$ ns relative to the excitation laser pulse and gate widths of $\delta t = 30$ µs for signal accumulation. For determination of the luminescence decay kinetics, the initial gate delay was stepwise increased and was used for the construction of the intensity–time traces. Typically, 300 spectra were recorded and used in determining the luminescence decay kinetics. For the laser-power-dependent luminescence measurements, a set of absorptive gray filters and a power meter FieldMax 2-TOP with connected PowerMax PM10V1 (Coherent, Portland, OR, USA) were used. The luminescence decay kinetics were evaluated by using the following equation [Eq. (2)]:

$$I(t) = A + B_1 \bullet exp\left(\frac{-t}{\tau_1}\right) + B_2 \bullet exp\left(\frac{-t}{\tau_2}\right) \qquad (2)$$

in which τ_1 and τ_2 represent the luminescence decay times. From the coefficients B_1 and B_2, the relative fractions α_1 and α_2 were calculated according to the following equation [Eq. (3)]:

$$\alpha_1 = \frac{B_1 \bullet \tau_1}{(B_1 \bullet \tau_1 + B_2 \bullet \tau_2)} \quad (3)$$

The average decay time (τ_m) was calculated by the following equation [Eq. (4)]:

$$\tau_m = \frac{\sum_{i=1}^{z} B_i \tau_i^2}{\sum_{i=1}^{z} B_i \tau_i} \quad (4)$$

Acknowledgements

We thank Andrea Scholz and Janine Partsch for excellent technical assistance. This work was supported by the Helmholtz Initiative and Networking Fund [Functional Nanomaterials for Multimodality Cancer Imaging (NanoTracking), project ID: VH-VI-421], a Helmholtz-Zentrum Dresden-Rossendorf fellowship to M.S., and an Alexander von Humboldt Foundation research fellowship to T.J.

Conflict of Interest

The authors declare no conflict of interest.

Keywords: core–shell materials · lanthanides · nanostructures · photoluminescence · upconversion

[1] F. Auzel, *Chem. Rev.* **2004**, *104*, 139 – 173.
[2] G. Chen, H. Qiu, P. N. Prasad, X. Chen, *Chem. Rev.* **2014**, *114*, 5161 – 5214.
[3] A. Gnach, T. Lipinski, A. Bednarkiewicz, J. Rybka, J. A. Capobianco, *Chem. Soc. Rev.* **2015**, *44*, 1561 – 1584.
[4] L. Prodi, E. Rampazzo, F. Rastrelli, A. Speghini, N. Zaccheroni, *Chem. Soc. Rev.* **2015**, *44*, 4922 – 4952.
[5] A. Escudero, A. I. Becerro, C. Carrillo-Carrión, N. O. Núñez, M. V. Zyuzin, M. Laguna, D. González-Mancebo, M. Ocaña, W. J. Parak, *Nanophotonics* **2017**, *6*, 881 – 921.
[6] H. H. Gorris, U. Resch-Genger, *Anal. Bioanal. Chem.* **2017**, *409*, 5875 – 5890.
[7] A. Gulzar, J. T. Xu, P. P. Yang, F. He, L. G. Xu, *Nanoscale* **2017**, *9*, 12248 – 12282.
[8] X. Liu, C.-H. Yan, J. A. Capobianco, *Chem. Soc. Rev.* **2015**, *44*, 1299 – 1301.
[9] D. Mendez-Gonzalez, E. Lopez-Cabarcos, J. Rubio-Retama, M. Laurenti, *Adv. Colloid Interface Sci.* **2017**, *249*, 66 – 87.
[10] U. Resch-Genger, H. H. Gorris, *Anal. Bioanal. Chem.* **2017**, *409*, 5855 – 5874.
[11] D. M. Wang, B. Liu, Z. W. Quan, C. X. Li, Z. Y. Hou, B. G. Xing, J. Lin, *J. Mater. Chem. B* **2017**, *5*, 2209 – 2230.
[12] S. Wilhelm, *ACS Nano* **2017**, *11*, 10644 – 10653.
[13] X. J. Zhu, Q. Q. Su, W. Feng, F. Y. Li, *Chem. Soc. Rev.* **2017**, *46*, 1025 – 1039.
[14] J. A. Damasco, G. Y. Chen, W. Shao, H. Agren, H. Y. Huang, W. T. Song, J. F. Lovell, P. N. Prasad, *ACS Appl. Mater. Interfaces* **2014**, *6*, 13884 – 13893.
[15] M. Haase, H. Schafer, *Angew. Chem. Int. Ed.* **2011**, *50*, 5808 – 5829; *Angew. Chem.* **2011**, *123*, 5928 – 5950.
[16] C. S. Mao, X. H. Yang, L. J. Zhao, *Chem. Eng. J.* **2013**, *229*, 429 – 435.
[17] F. Wang, Y. Han, C. S. Lim, Y. H. Lu, J. Wang, J. Xu, H. Y. Chen, C. Zhang, M. H. Hong, X. G. Liu, *Nature* **2010**, *463*, 1061 – 1065.
[18] D. Q. Chen, M. Xu, M. F. Ma, P. Huang, *Dalton Trans.* **2017**, *46*, 15373 – 15385.
[19] P. Du, A. M. Deng, L. H. Luo, J. S. Yu, *New J. Chem.* **2017**, *41*, 13855 – 13861.
[20] P. Du, P. Zhang, S. H. Kang, J. S. Yu, *Sens. Actuators B* **2017**, *252*, 584 – 591.
[21] M. Y. Hossan, A. Hor, Q. Luu, S. J. Smith, P. S. May, M. T. Berry, *J. Phys. Chem. C* **2017**, *121*, 16592 – 16606.
[22] M. Kaiser, C. Wurth, M. Kraft, I. Hyppanen, T. Soukka, U. Resch-Genger, *Nanoscale* **2017**, *9*, 10051 – 10058.
[23] U. Kostiv, V. Lobaz, J. Kucka, P. Svec, O. Sedlacek, M. Hruby, O. Janouskova, P. Francova, V. Kolarova, L. Sefc, D. Horak, *Nanoscale* **2017**, *9*, 16680 – 16688.
[24] A. Pilch, C. Wurth, M. Kaiser, D. Wawrzynczyk, M. Kurnatowska, S. Arabasz, K. Prorok, M. Samoc, W. Strek, U. Resch-Genger, A. Bednarkiewicz, *Small* **2017**, *13*, 1701635.
[25] S. Dühnen, T. Rinkel, M. Haase, *Chem. Mater.* **2015**, *27*, 4033 – 4039.
[26] N. J. J. Johnson, W. Oakden, G. J. Stanisz, R. S. Prosser, F. C. J. M. van Veggel, *Chem. Mater.* **2011**, *23*, 4877 – 4877.
[27] X. M. Li, D. K. Shen, J. P. Yang, C. Yao, R. C. Che, F. Zhang, D. Y. Zhao, *Chem. Mater.* **2013**, *25*, 106 – 112.
[28] B. Voss, M. Haase, *ACS Nano* **2013**, *7*, 11242 – 11254.
[29] B. Voss, J. Nordmann, A. Uhl, R. Komban, M. Haase, *Nanoscale* **2013**, *5*, 806 – 812.
[30] A. D. Ostrowski, E. M. Chan, D. J. Gargas, E. M. Katz, G. Han, P. J. Schuck, D. J. Milliron, B. E. Cohen, *ACS Nano* **2012**, *6*, 2686 – 2692.
[31] M. Banski, M. Afzaal, A. Podhorodecki, J. Misiewicz, A. L. Abdelhady, P. O'Brien, *J. Nanopart. Res.* **2012**, *14*, 1228.
[32] M. Banski, A. Podhorodecki, J. Misiewicz, M. Afzaal, A. L. Abdelhady, P. O'Brien, *J. Mater. Chem. C* **2013**, *1*, 801 – 807.
[33] J. Shan, X. Qin, N. Yao, Y. Ju, *Nanotechnology* **2007**, *18*, 445607.
[34] G. F. Wang, W. P. Qin, J. S. Zhang, L. L. Wang, G. D. Wei, P. F. Zhu, R. J. Kim, *J. Alloys Compd.* **2009**, *475*, 452 – 455.
[35] Y. S. Chen, W. He, Y. C. Jiao, H. H. Wang, X. L. Hao, J. X. Lu, S. E. Yang, *J. Lumin.* **2012**, *132*, 2247 – 2250.
[36] H. Dong, S. R. Du, X. Y. Zheng, G. M. Lyu, L. D. Sun, L. D. Li, P. Z. Zhang, C. Zhang, C. H. Yan, *Chem. Rev.* **2015**, *115*, 10725 – 10815.
[37] D. T. Klier, M. U. Kumke, *J. Mater. Chem. C* **2015**, *3*, 11228 – 11238.
[38] S. Asokan, K. M. Krueger, A. Alkhawaldeh, A. R. Carreon, Z. Z. Mu, V. L. Colvin, N. V. Mantzaris, M. S. Wong, *Nanotechnology* **2005**, *16*, 2000 – 2011.
[39] N. Gresty, O. Masala, C. Newman, S. Whitelegg, N. Pickett (Nanoco Technologies), Patent US20140011317 A1, **2014**.
[40] W. Y. L. Ko, H. G. Bagaria, S. Asokan, K.-J. Lin, M. S. Wong, *J. Mater. Chem.* **2010**, *20*, 2474 – 2478.
[41] J. Shen, G. Y. Chen, A. M. Vu, W. Fan, O. S. Bilsel, C. C. Chang, G. Han, *Adv. Opt. Mater.* **2013**, *1*, 644 – 650.
[42] Y. T. Zhong, G. Tian, Z. J. Gu, Y. J. Yang, L. Gu, Y. L. Zhao, Y. Ma, J. N. Yao, *Adv. Mater.* **2014**, *26*, 2831 – 2837.
[43] Y. Zhang, Z. Z. Yu, J. Q. Li, Y. X. Ao, J. W. Xue, Z. P. Zeng, X. L. Yang, T. T. Y. Tan, *ACS Nano* **2017**, *11*, 2846 – 2857.
[44] Q. Liu, Y. Sun, T. S. Yang, W. Feng, C. G. Li, F. Y. Li, *J. Am. Chem. Soc.* **2011**, *133*, 17122 – 17125.
[45] R. Naccache, Q. Yu, J. A. Capobianco, *Adv. Opt. Mater.* **2015**, *3*, 482 – 509.
[46] C. Yan, H. Zhao, D. F. Perepichka, F. Rosei, *Small* **2016**, *12*, 3888 – 3907.
[47] X. S. Zhai, S. S. Liu, Y. L. Zhang, G. S. Qin, W. P. Qin, *J. Mater. Chem. C* **2014**, *2*, 2037 – 2044.
[48] P. Huang, W. Zheng, S. Zhou, D. Tu, Z. Chen, H. Zhu, R. Li, E. Ma, M. Huang, X. Chen, *Angew. Chem. Int. Ed.* **2014**, *53*, 1252 – 1257; *Angew. Chem.* **2014**, *126*, 1276 – 1281.
[49] H.-X. Mai, Y.-W. Zhang, L.-D. Sun, C.-H. Yan, *J. Phys. Chem. C* **2007**, *111*, 13730 – 13739.
[50] F. Vetrone, R. Naccache, V. Mahalingam, C. G. Morgan, J. A. Capobianco, *Adv. Funct. Mater.* **2009**, *19*, 2924 – 2929.
[51] L. Lei, B. Xie, Y. Li, J. Zhang, S. Xu, *J. Lumin.* **2017**, *190*, 462 – 467.
[52] M. Quintanilla, F. Ren, D. Ma, F. Vetrone, *ACS Photonics* **2014**, *1*, 662 – 669.
[53] X. Huang, J. Lin, *J. Mater. Chem. C* **2015**, *3*, 7652 – 7657.
[54] S. Hao, G. Chen, C. Yang, W. Shao, W. Wei, Y. Liu, P. N. Prasad, *Nanoscale* **2017**, *9*, 10633 – 10638.
[55] X. Du, X. Wang, L. Meng, Y. Bu, X. Yan, *Nanoscale Res. Lett.* **2017**, *12*, 163.

[56] S. Han, R. Deng, X. Xie, X. Liu, *Angew. Chem. Int. Ed.* **2014**, *53*, 11702 – 11715; *Angew. Chem.* **2014**, *126*, 11892 – 11906.
[57] R. R. Qiao, C. H. Liu, M. H. Liu, H. Hu, C. Y. Liu, Y. Hou, K. C. Wu, Y. N. Lin, J. M. Liang, M. Y. Gao, *ACS Nano* **2015**, *9*, 2120 – 2129.
[58] L. L. Wang, X. J. Xue, H. Chen, D. Zhao, W. P. Qin, *Chem. Phys. Lett.* **2010**, *485*, 183 – 186.
[59] Q. Zhang, B. Yan, *Chem. Commun.* **2011**, *47*, 5867 – 5869.
[60] D. D. Ma, L. J. Meng, Y. Z. Chen, M. Hu, Y. K. Chen, C. Huang, J. Shang, R. F. Wang, Y. M. Guo, J. Yang, *ACS Appl. Mater. Interfaces* **2015**, *7*, 16257 – 16265.
[61] J. X. Wang, T. Ming, Z. Jin, J. F. Wang, L. D. Sun, C. H. Yan, *Nat. Commun.* **2014**, *5*, 5669.
[62] X. Xu, Z. Wang, P. P. Lei, Y. N. Yu, S. Yao, S. Y. Song, X. L. Liu, Y. Su, L. L. Dong, J. Feng, H. J. Zhang, *ACS Appl. Mater. Interfaces* **2015**, *7*, 20813 – 20819.
[63] L. A. Feigin, D. I. Svergun, *Structure Analysis by Small-Angle X-ray and Neutron Scattering*, Springer, New York, **1987**.
[64] T. Ben-Nun, A. Ginsburg, P. Szekely, U. Raviv, *J. Appl. Crystallogr.* **2010**, *43*, 1522 – 1531.
[65] W. Yu, W. Xu, H. W. Song, S. Zhang, *Dalton Trans.* **2014**, *43*, 6139 – 6147.
[66] W. Zheng, P. Huang, D. T. Tu, E. Ma, H. M. Zhu, X. Y. Chen, *Chem. Soc. Rev.* **2015**, *44*, 1379 – 1415.
[67] C. Würth, M. Kaiser, S. Wilhelm, B. Grauel, T. Hirsch, U. Resch-Genger, *Nanoscale* **2017**, *9*, 4283 – 4294.
[68] D. M. Liu, X. X. Xu, Y. Du, X. Qin, Y. H. Zhang, C. S. Ma, S. H. Wen, W. Ren, E. M. Goldys, J. A. Piper, S. X. Dou, X. G. Liu, D. Y. Jin, *Nat. Commun.* **2016**, *7*, 10254.
[69] J. G. E. Bünzli, *Basics of Lanthanide Photophysics, Vol. 7*, Springer, Berlin, **2010**.
[70] The average decay time of $UCNP_{core}$ is composed of $\tau_1 = 46$ μs ($\alpha_1 = 81\%$) and $\tau_2 = 91$ μs ($\alpha_2 = 19\%$) for G1 + G2 as well as $\tau_1 = 61$ μs ($\alpha_1 = 87\%$) and $\tau_2 = 102$ μs ($\alpha_2 = 13\%$) for R.
[71] A. Beeby, I. M. Clarkson, R. S. Dickins, S. Faulkner, D. Parker, L. Royle, A. S. de Sousa, J. A. G. Williams, M. Woods, *J. Chem. Soc. Perkin Trans. 2* **1999**, 493 – 503.
[72] F. Wang, R. R. Deng, J. Wang, Q. X. Wang, Y. Han, H. M. Zhu, X. Y. Chen, X. G. Liu, *Nat. Mater.* **2011**, *10*, 968 – 973.
[73] X. J. Xie, N. Y. Gao, R. R. Deng, Q. Sun, Q. H. Xu, X. G. Liu, *J. Am. Chem. Soc.* **2013**, *135*, 12608 – 12611.
[74] Y. F. Wang, G. Y. Liu, L. D. Sun, J. W. Xiao, J. C. Zhou, C. H. Yan, *ACS Nano* **2013**, *7*, 7200 – 7206.
[75] A. Skripka, R. Marin, A. Benayas, P. Canton, E. Hemmer, F. Vetrone, *Phys. Chem. Chem. Phys.* **2017**, *19*, 11825 – 11834.
[76] R. H. Page, K. I. Schaffers, P. A. Waide, J. B. Tassano, S. A. Payne, W. F. Krupke, W. K. Bischel, *J. Opt. Soc. Am. B* **1998**, *15*, 996 – 1008.
[77] B. D. Cullity, S. R. Stock, *Elements of X-ray Diffraction, 3rd ed.*, Prentice-Hall, New York, **2001**.

Received: November 20, 2017
Version of record online January 25, 2018

